Role of Indonesian Archipelago on Global Thermohaline Circulation: Insights from Numerical Experiments

Sandy Hardian Susanto Herho[1*], Iwan Pramesti Anwar[2, 3], Gisma Aminurah Firdaus[4], Dasapta Erwin Irawan[5], Rubiyanto Kapid[6]

[1*]Department of Earth and Planetary Sciences, University of California, Riverside, 92521, CA, USA.
[2]Samudera Sains Teknologi Research Institute, Bandung, 40151, West Java, Indonesia.
[3]Oceanography Research Group, Bandung Institute of Technology (ITB), Bandung, 40132, West Java, Indonesia.
[4]Indonesian Sugar Research Institute (P3GI), PT. Perkebunan Nusantara (PTPN) III, Pasuruan, 67126, East Java, Indonesia.
[5]Applied Geology Research Group, Bandung Institute of Technology (ITB), Bandung, 40132, West Java, Indonesia.
[6]Paleontology and Quaternary Geology Research Group, Bandung Institute of Technology (ITB), Bandung, 40132, West Java, Indonesia.

*Corresponding author. E-mail: sandy.herho@email.ucr.edu;

Abstract

This study employs the cGENIE Earth System Model to investigate the effects of the Indonesian Throughflow (ITF) and Indonesian Archipelago (IA) closure on global meridional thermohaline circulation (THC). Over a simulated period of 10,000 years, the analysis centers on critical variables, including surface density, vertical density profiles, global overturning circulation, and ocean ventilation age. The results reveal nuanced, non-statistically significant changes, emphasizing the regional influence of the ITF. Specifically, surface density anomalies manifest post-IA closure, notably in southern Mindanao and eastern Australia. Concurrently, anomalies in global overturning circulation indicate reduced vertical transport intensities in the Southern Ocean.

While cGENIE offers valuable insights, its limitations underscore the necessity for incorporating more complex climate models. This acknowledgment underscores the ongoing imperative to refine Earth System Models for a comprehensive understanding of the intricate interactions that shape global ocean dynamics and climate.

Keywords: cGENIE Earth System Model, Indonesian Archipelago, Indonesian Throughflow, Thermohaline Circulation

1 Introduction

Indonesia asserts its prominence as the world's largest archipelagic nation, strategically positioned at the confluence of Asia and Australia, bordered by the Indian Ocean and the Pacific Ocean. The Indonesian Archipelago (IA), comprising over 18,000 islands, traces its geological origins over 300 million years ago to intricate processes of subduction and collision during the Cenozoic era, resulting from the rearrangement of Gondwana fragments, extensively detailed in previous studies [1–3].

Within the field of climatology, the IA is commonly identified as the Maritime Continent (MC) [4], strategically located in the western Pacific region, specifically within the Indo-Pacific Warm Pool (IPWP) [5]. Recognized as a substantial source of latent heat release in the atmosphere, the MC plays a critical role in initiating deep convection processes that intricately govern both the Hadley and Walker circulations within tropical regions [6, 7]. Consequently, the region stands out for harboring the most robust monsoonal activity on Earth [8]. Additionally, the MC assumes a pivotal role in global atmosphere–ocean interactions, exerting influence over phenomena such as the El Niño Southern Oscillation (ENSO) [9], Indian Ocean Dipole mode (IOD) [10], and Madden–Julian Oscillation (MJO) [11].

Oceanographically, the IA plays an important role, serving as the sole conduit for the transit of water masses from the Pacific Ocean to the Indian Ocean [12–15]. This transport process is recognized as the Indonesian Throughflow (ITF), which also represents the only low-latitude current connecting major ocean basins in the present-day [16]. On an annual time scale, the ITF transfers approximately 0 - 30 Sv (1 Sv $\equiv 10^6$ m^3/s) of water mass, as estimated by various numerical models and observations [e. g., 12, 17–33]. Heat transfer through the ITF, based on estimates from the Global Climate Model (GCM) conducted by Hirst and Godfrey [25], is approximately 0.63 PW. This value represents approximately one-third of the total heat input in the equatorial Pacific region.

The ITF facilitates the transfer of warm, low-salinity water masses from the west equatorial Pacific Ocean to the east equatorial Indian Ocean through a defined route encompassing the Makassar Strait, Maluku Sea, and Halmahera Sea [15, 33–36]. In this context, the Makassar Strait is recognized as the primary entry point for the ITF. The water mass originating from the North Pacific navigates through the Celebes Sea before proceeding towards the Makassar Strait and the IA. Upon entering the IA, the current from the Makassar Strait bifurcates into two branches, one traversing southwest Indonesia, and the other moving towards the Indian Ocean through the Lombok Strait. Simultaneously, another branch moves eastward in the Indonesian region, specifically into the Banda Sea via the Flores Sea.

Within the Banda Sea, a complex mixing process unfolds as water masses originating from the South Pacific, entering through the Halmahera Sea, Maluku Sea, and Seram Sea, interact. This amalgamation of water masses in the Banda Sea subsequently progresses towards the Indian Ocean through the Ombai Strait and Timor Gap. The Maluku Sea stands as the second pivotal gateway for the ITF. Pacific water masses traverse the Maluku Sea to reach the Seram Sea via the Lifamatola Strait. From the Seram Sea, they continue their trajectory through the Manipa Strait towards the Banda Sea.

The Halmahera Sea represents the third key entry point for the ITF, with South Pacific water masses transiting through this sea towards the Seram Sea and the Aru Basin. Following a mixing process with water masses originating from the Banda Sea, the combined water mass moves towards the Indian Ocean via the eastern part of the Timor Sea.

On intra-annual, annual, and inter-annual time scales, the ITF is influenced and, in turn, also influences tidal movements, monsoons, and atmosphere-ocean interactions such as ENSO and IOD. Additionally, the ITF may be affected by decadal variability in the Pacific [33, 34, 36]. However, on a centennial time scale, the commonly used Island Rule theory [15], employed to estimate the strength of the ITF, failed to indicate a weakening trend based on Coupled Model Intercomparison Project phase 5 (CMIP5) multimodel simulations [37]. This limitation arises because the Island Rule solely calculates the strength of the ITF as a line integral of wind stress and Coriolis terms along a defined boundary (dominated by wind-driven forces) without accounting for the long-term circulation of heat flux and freshwater. This long-term circulation induces interior mixing of temperature and salinity, known as thermohaline circulation (THC). Therefore, to present a realistic centennial projection, an additional term accounting for the contribution of THC in the Pacific is necessary, as demonstrated in the Ocean Forecasting Australia Model version 3 (OFAM3) simulation [38].

Apart from the temporal regulation of the ITF by wind-driven circulation, the THC has long been acknowledged as a contributing factor to the ITF's strength within the upper segment of the global overturning circulation scheme [13]. The trajectory of the warm surface water initiates from the North Pacific Deep Water (NPDW), extending through the IA into the Indian Ocean. Within the $10-20°$S belt of the Indian Ocean, a complex mixing of Pacific and Indian Ocean water occurs. The southward journey then proceeds through the Mozambique Channel, where it divides into two primary flows. The dominant portion, comprising Agulhas Current system, enters the Agulhas Retroflection into the Southern Ocean, while the remaining stream finds its way into the Atlantic.

Meanwhile, at the western boundary of the Indian Ocean, the convergence of northward and southward boundary currents facilitates the closure of tropical and subtropical gyres, aligning with the observations of Hughes et al. [39]. These gyres actively contribute to pumping water into the Antarctic Circumpolar Current (ACC) and the South Atlantic Gyre, a pivotal process in the formation of North Atlantic Deep

Water (NADW), as detailed by Toole and Warren [24]. Notably, the ITF enhances the meridional steric height gradient, thereby influencing the strength of these gyres. The complex interplay implies that the ITF, in addition to its role in balancing the thermal and saline conditions between the Pacific and the Indian Ocean, might also have a pronounced influence on the physical conditions of the distant Atlantic. This cyclical process aligns with the concept known as the great ocean conveyor belt hypothesis [40], which was deemed accountable for abrupt climate changes during glacial-interglacial periods [e. g., 41–45].

Given the observed weakening trend in the Atlantic Meridional Overturning Circulation (AMOC) [e. g., 46–49], the principal driver of the modern THC, and its potential correlation with a density-driven weakening of the ITF due to recent anthropogenic climate change [37, 38, 50, 51], a comprehensive understanding of the ITF's role in this circulation becomes imperative. This study employs classical numerical experiments, with a focus on the blockage of the IA, aiming to unravel the geographic significance of both IA and ITF in the global meridional THC.

In contrast to prior numerical experiments [16, 52–54] that concentrated on the short-term analysis of IA closure's impact on the surface ocean, influencing climate, and featured a limited simulation time of up to 105 years [16], our approach prioritizes a more extended physical realization of the ocean. Although this method adopts low spatial resolution, it extends over a more extended simulation time, facilitating the attainment of quasi-steady-state conditions (equilibrium numerical solutions). This extended duration enables the analysis of the global meridional THC on a centennial time scale, providing valuable insights into the long-term dynamics of the circulation system.

2 Materials and Methods

2.1 Numerical Experiments

This study employed the carbon-centric Grid Enabled Integrated Earth system model (cGENIE) muffin version (hereafter referred to as cGENIE) [55]. cGENIE, classified as an Earth system model of intermediate complexity (EMIC), served as a bridge between theoretical/conceptual models and GCMs [56]. EMICs prioritize computational efficiency and speed, making them well-suited for the investigation of long-term climate phenomena, like THC [57].

cGENIE offers the advantage of compartmentalizing each Earth system, providing flexibility for addressing specific research questions [58]. The model comprises seven components, including the GOLDSTEIN, which manages the physical dynamics of the atmosphere, ocean, and sea ice [55, 59]. Other components include BIOGEM for marine biogeochemical dynamics [60], ATCHEM for atmospheric chemistry [58], ENTS for land surface and carbon cycle processes [61], ROKGEM for terrestrial rock weathering [62], SEDGEM for ocean sedimentation [63], ECOGEM for plankton ecological dynamics [64], and GENIE-PLASIM for fully coupled intermediate complexity Atmosphere–Ocean General Circulation Model (AOGCM) [65]. The calibration of GOLDSTEIN parameters was conducted utilizing the ensemble Kalman filter (EnKF) methodology [66], aligning them with annual mean climatological measurements of temperature, salinity, surface air temperature, and humidity [60].

The oceanic component within cGENIE employs a 3D frictional geostrophic ocean model, wherein the representation of ocean physics is based on the ocean fluid approximation method derived by Edwards et al. [67]. This model has undergone rigorous testing, demonstrating its capability to simulate multiple stable states of the THC [68]. Additionally, in the latest update, this model has incorporated ITF within its framework [55]. cGENIE also demonstrated the capability to produce realistic THC hysteresis features, as discussed by Lenton et al. [69].

The 2D Atmospheric Energy-Moisture Balance Model (EMBM), aligned with the UVic Earth system model [70] and utilizing air temperature and specific humidity as forecast tracers, comprehensively accounts for the heat and moisture balance within the atmospheric boundary layer. The exchange of heat and moisture with ocean and land surfaces, coupled with the ENTS module, is facilitated through horizontal mixing throughout the atmosphere, with precipitation triggered above a specified relative humidity threshold.

The sea-ice model, designed after the sea-ice component of the UVic Earth system model, integrates ice thickness, areal fraction, and concentration as prognostic variables. This allows for the systematic tracking of horizontal sea-ice movement and the exchange of heat and fresh water with both the ocean and atmosphere. Detailed insights into the model and its coupling processes are available in Marsh et al.[55].

In the course of our numerical experiments, we employed an ocean model distinguished by its robust configuration. The model's specifications encompassed a resolution defined by 36×36 equal-area grids, translating to a grid size of $10° \times 10°$. This grid architecture, characterized by uniformity in both longitude and the sine of latitude, facilitated a meticulous examination of the targeted oceanographic phenomena. Notably, the ocean model featured 16 logarithmically-spaced depth levels, strategically positioned to capture the nuances of the ocean's vertical structure. These depth levels were meticulously distributed at intervals of 40.42 m, 127.552 m, 228.77 m, 346.354 m, 482.949 m, 641.629 m, 825.964 m, 1040.103 m, 1288.865 m, 1577.846 m, 1913.551 m, 2303.532 m, 2756.567 m, 3282.848 m, 3894.22 m, and 4604.439 m.

The initial conditions were established based on a resting ocean configuration with a uniform distribution of temperature and salinity, following the framework proposed by Manabe and Bryan [71], detailed by Cao et al. [72]. For boundary conditions, HadCM3 outputs [73] were utilized, coarsely regridded into cGENIE grids through the muffingen software [74]. Continental configuration was also generated using muffingen.

Atmospheric CO_2 forcing was set at pre-industrial levels of 278 ppm. To calculate ocean ventilation age in this experiment, a transient dye tracer methodology introduced by England [75] was employed. The control experiment featured an open configuration of the IA, while the test experiment involved closing the IA. For each of these experiments, we used a 10,000-year simulation time.

2.2 Data Analysis

In this study, we analyzed vertical and horizontal annual density profiles, while also examining the vertical streamfunction profile depicting the global overturning circulation. Additionally, we investigated the vertical profile of ocean ventilation age. These three variables—vertical and horizontal density profiles, along with vertical profiles of streamfunction and ocean ventilation age—played crucial roles in estimating and assessing the global meridional THC.

We utilized non-parametric statistical methods, specifically the Mann–Whitney U (MWU) and two-sample Kolmogorov-Smirnov (KS) tests, to quantify the disparities between test and control experiments. These tests were chosen for their applicability to variables that may not adhere to a Gaussian distribution, a characteristic often encountered in the field of oceanography [e. g., 76–78]. Notably, their effectiveness in climate science applications has been demonstrated in prior studies [e. g., 52, 79–83].

Before conducting these tests, a pre-processing step involved transforming the 2D model outputs into a 1D array using xarray [84] and NumPy [85] libraries in Python. In this array, each member represented individual grids in the model outputs. This approach ensured a coherent and standardized comparison between the experimental scenarios.

Following data pre-processing, the MWU test was employed to compute the sum of ranks for each group, resulting in U_X for the control dataset and U_Y for the test dataset. The test statistic (U) was then determined as the smaller of the two sums.

Under the null hypothesis, the expected value of U was given by:

$$E(U) = \frac{n_X(n_X + n_Y + 1)}{2} \tag{1}$$

The variance of U under the null hypothesis was calculated using the formula:

$$\mathrm{Var}(U) = \frac{n_X n_Y(n_X + n_Y + 1)}{12} \tag{2}$$

Subsequently, the $Z-$statistic was computed:

$$Z = \frac{U - E(U)}{\sqrt{\mathrm{Var}(U)}} \tag{3}$$

Comparing the $Z-$statistic to critical values from the standard normal distribution or converting it to a p-value, in this study we used 0.05 as the significance criteria, facilitates the determination of the statistical significance of differences between the control and test datasets.

To extend the analysis, the two-sample KS test was applied to assess the distributional differences between the control (X) and test (Y) datasets. The procedure began by sorting the combined data and calculating the empirical distribution functions (ECDFs) for both groups.

The KS test statistic (D) was then computed as the maximum absolute vertical deviation between the two ECDFs:

$$D = \max |F_X(x) - F_Y(x)| \tag{4}$$

Under the null hypothesis that the two samples were drawn from the same distribution, the distribution of the test statistic was independent of the underlying cumulative distribution functions. Consequently, critical values or p-values 0.05 were used to determine the statistical significance of the observed differences.

For our sample sizes, the asymptotic distribution of D was approximated by:

$$D\sqrt{\frac{n_X n_Y}{n_X + n_Y}} \tag{5}$$

, where n_X and n_Y are the sample sizes of the control and test datasets, respectively. The comparison of the observed test statistic to critical values or the conversion to a p-value allows for the evaluation of the statistical significance of distributional disparities between the two samples. The execution of these two statistical tests was conducted using the SciPy library [86] in Python.

3 Results and Discussion

In Figure 1, the annual average global surface density profiles over a 10,000-year period illustrate noteworthy patterns. With the IA open, the average surface density stands at 1025.37 kg/m^3, peaking at 1027.796 kg/m^3 in the Bellingshausen Sea, part of the Southern Ocean near West Antarctica. Conversely, the lowest density of 1022.16 kg/m^3 is observed in the Maluku Sea, Indonesia. Closure of the IA induces only a marginal change, resulting in a slight decrease in the global average surface density by -0.01 kg/m^3.

Notable alterations are evident with a surface density increase of 0.451 kg/m^3 in the Coral Sea, northeast of Australia, and a decrease of -0.666 kg/m^3 in the Celebes Sea, south of Mindanao, Philippines. However, statistical analyses via the MWU and KS tests fail to provide enough evidence to reject the null hypothesis, suggesting that IA closure does not significantly impact global surface density (both tests yielding a p-value > 0.05).

Moving to Figure 2, which presents the annual average global vertical density profile, distinct patterns emerge. In the control run, the highest average vertical density is 1027.221 kg/m^3, contrasting with 1023.706 kg/m^3 in the test run. The location with the maximum density (1027.829 kg/m^3 with the IA open, and 1027.832 kg/m^3 with the IA closed) is found at 76.46°S and a depth of 2757 m, while the minimum density (1023.706 kg/m^3 with the IA open, and 1023.791 kg/m^3 with the IA closed) is recorded at 1.592°N and a depth of 40.42 m. Despite these variations, the global difference in vertical density following IA closure remains minute at -0.003 kg/m^3.

The most significant density increase of 0.092 kg/m^3 occurs at 11.21°S and a depth of 127.6 m, while the most substantial decrease of -0.072 kg/m^3 is noted at 21.17°N and a depth of 40.42 m. Statistically, no significant differences are detected in the vertical density profile, with both the MWU and KS tests yielding a p-value > 0.05.

Transitioning to Figure 3, an in-depth examination of the average annual global overturning circulation profiles with varying IA states is presented. In the open IA state, the average circulation is quantified at 0.997 Sv, reaching a maximum of 53.913 Sv at 41.81°S and a depth of 80.84 m, and a minimum of -42.034 Sv at 12.84°S and the same depth. Upon IA closure, a discernible average increase in global overturning circulation is recorded, totaling 0.245 Sv. This increase is most pronounced at 46.24°S and a depth of 1426 m, reaching 2.906 Sv. In contrast, the most significant decrease is noted at 56.44°S and a depth of 2520 m, registering -2.802 Sv. It is noteworthy that positive values denote counterclockwise circulation, while negative values signify clockwise circulation.

Statistically, results from both the MWU and KS tests indicate no significant change in overall global overturning circulation, with each test yielding a p-value > 0.05.

Figure 4 provides insights into the dynamics of annual ventilation age transects under different IA states. In the open IA state, the average ventilation age is 393.67 years, peaking at 1167.713 years at 59.44°N and a depth of 1578 m, and reaching a minimum of 0.04 years at 21.17°N and a depth of 40.42 m. Upon IA closure, the global average ventilation age decreases by -13,924 years. The most significant increase in ventilation age, amounting to 15,225 years, occurs at 14.48°S and a depth of 641.6 m. Conversely, the most substantial decrease of -62,673 years is observed at 7.984°S and a depth of 1578 m. However, no significant difference is detected in vertical ventilation age conditions, as neither the MWU nor KS tests reveal a statistically significant distinction (p-value > 0.05).

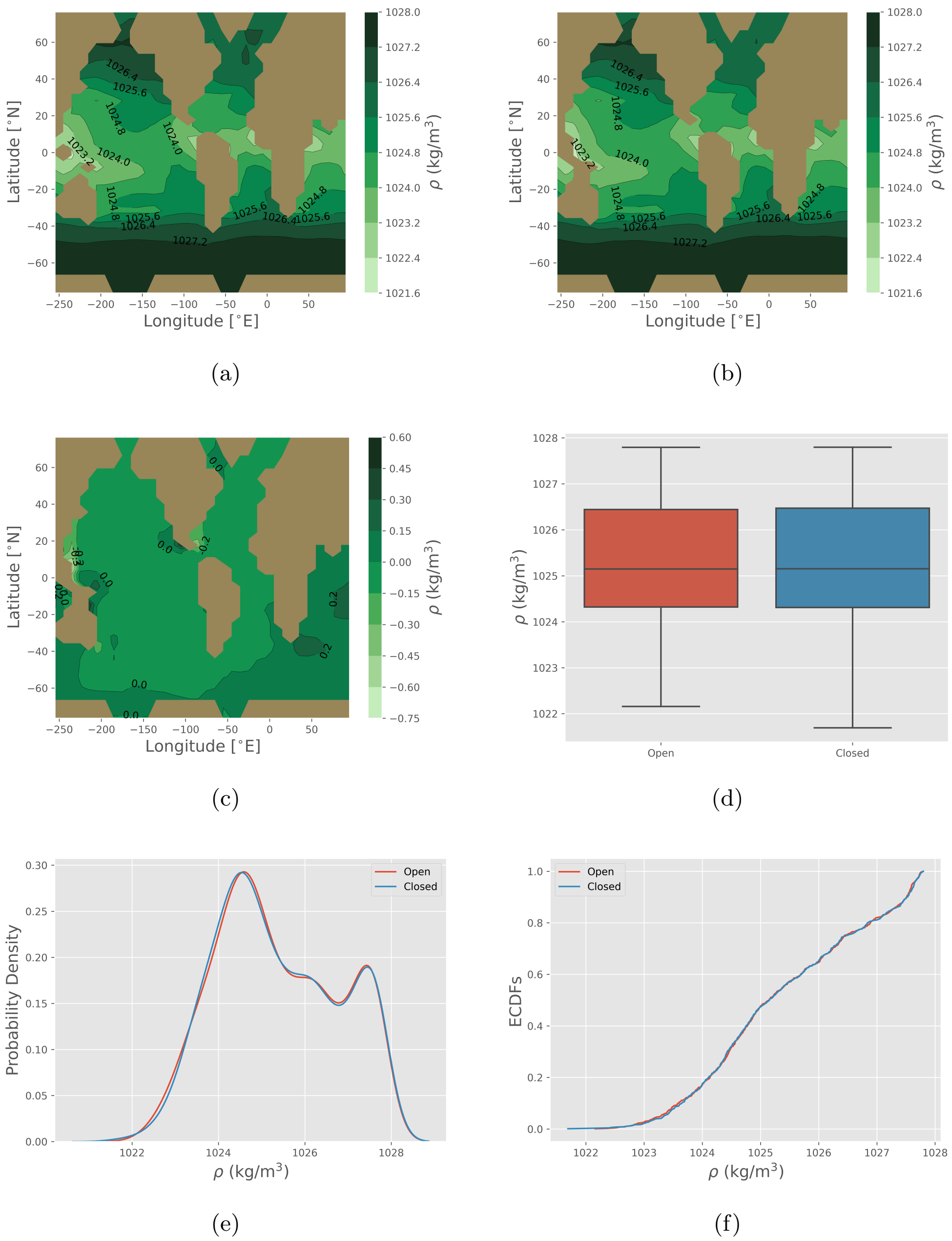

Fig. 1: Global sea surface density profiles under two distinct states: (a) the open IA state representing the control experiment and (b) the closed IA state depicting the test experiment. The disparities between these two scenarios are visually highlighted through various components: (c) field anomalies presenting the differences (test - control), (d) box plots offering a statistical overview of the density differences, (e) Kernel Density Estimates (KDEs) providing a smoothed distribution of the density differences, and (f) ECDFs illustrating the cumulative probability distribution of the density differences. These graphs were processed using Matplotlib[87] and seaborn [88] libraries in Python.

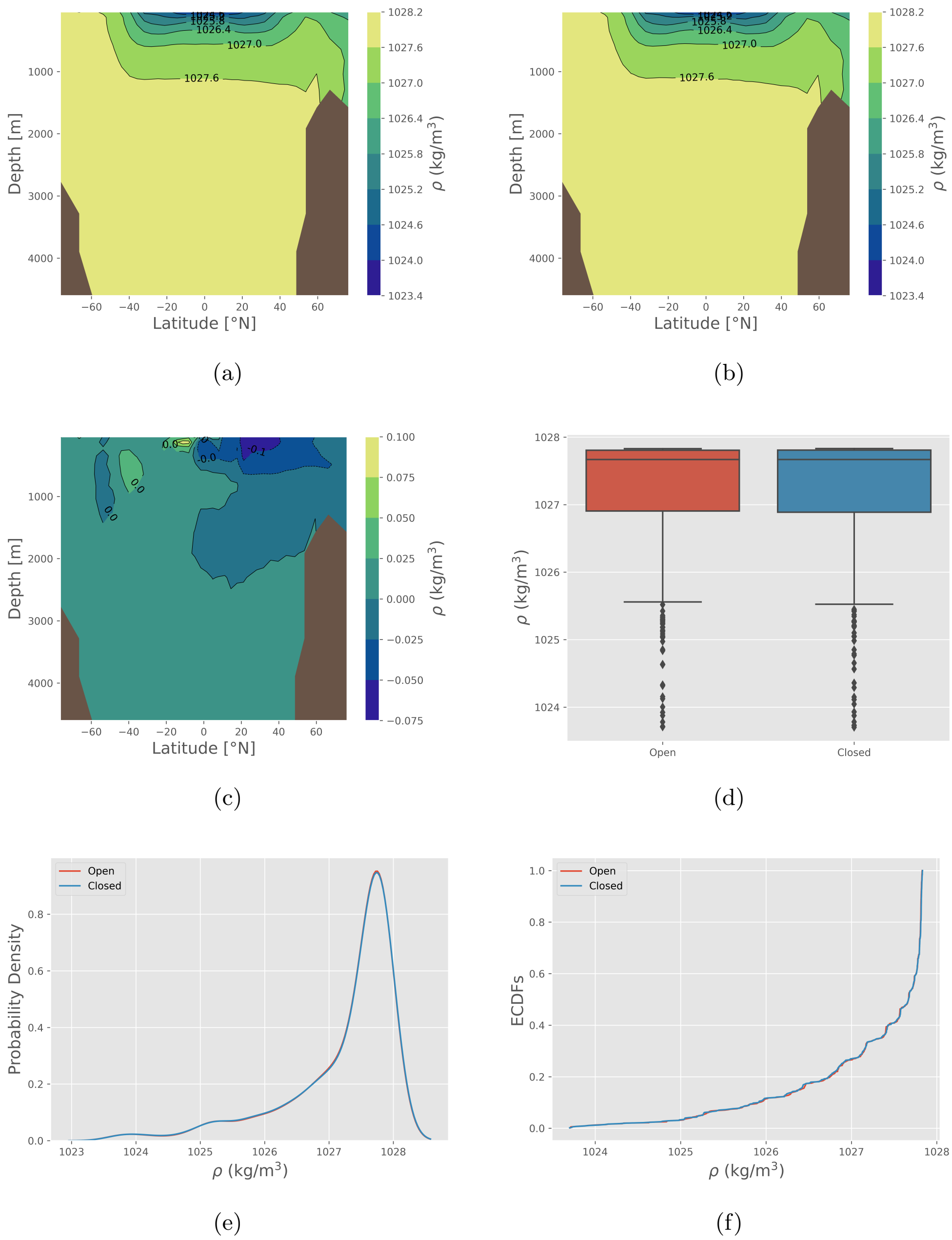

Fig. 2: Same as Figure 1, but for zonally averaged vertical density profiles.

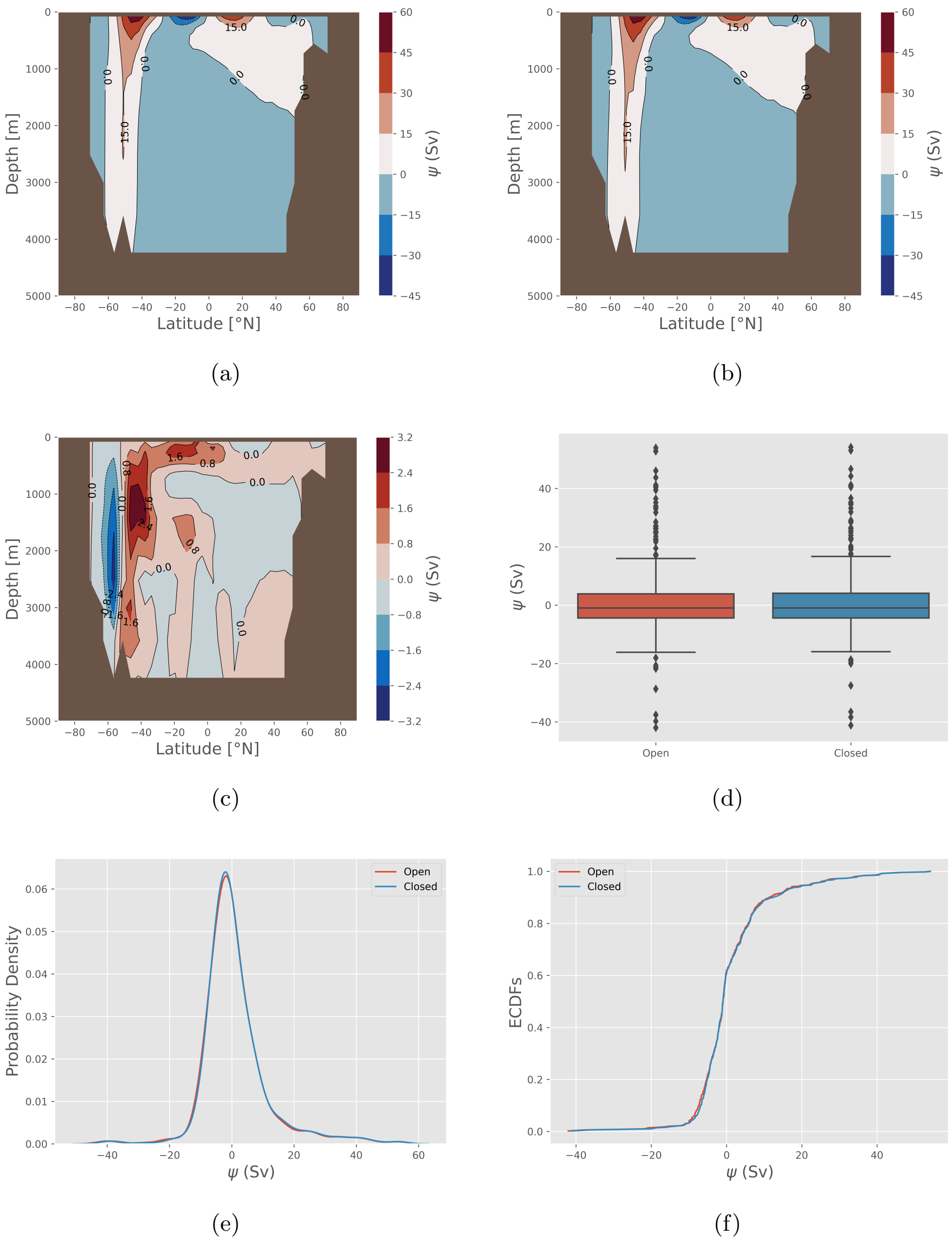

Fig. 3: Same as Figures 1 and 2 but for global overturning circulation. Streamfunctions exhibiting a counterclockwise rotation are denoted by positive values, whereas those with a clockwise rotation are assigned negative values.

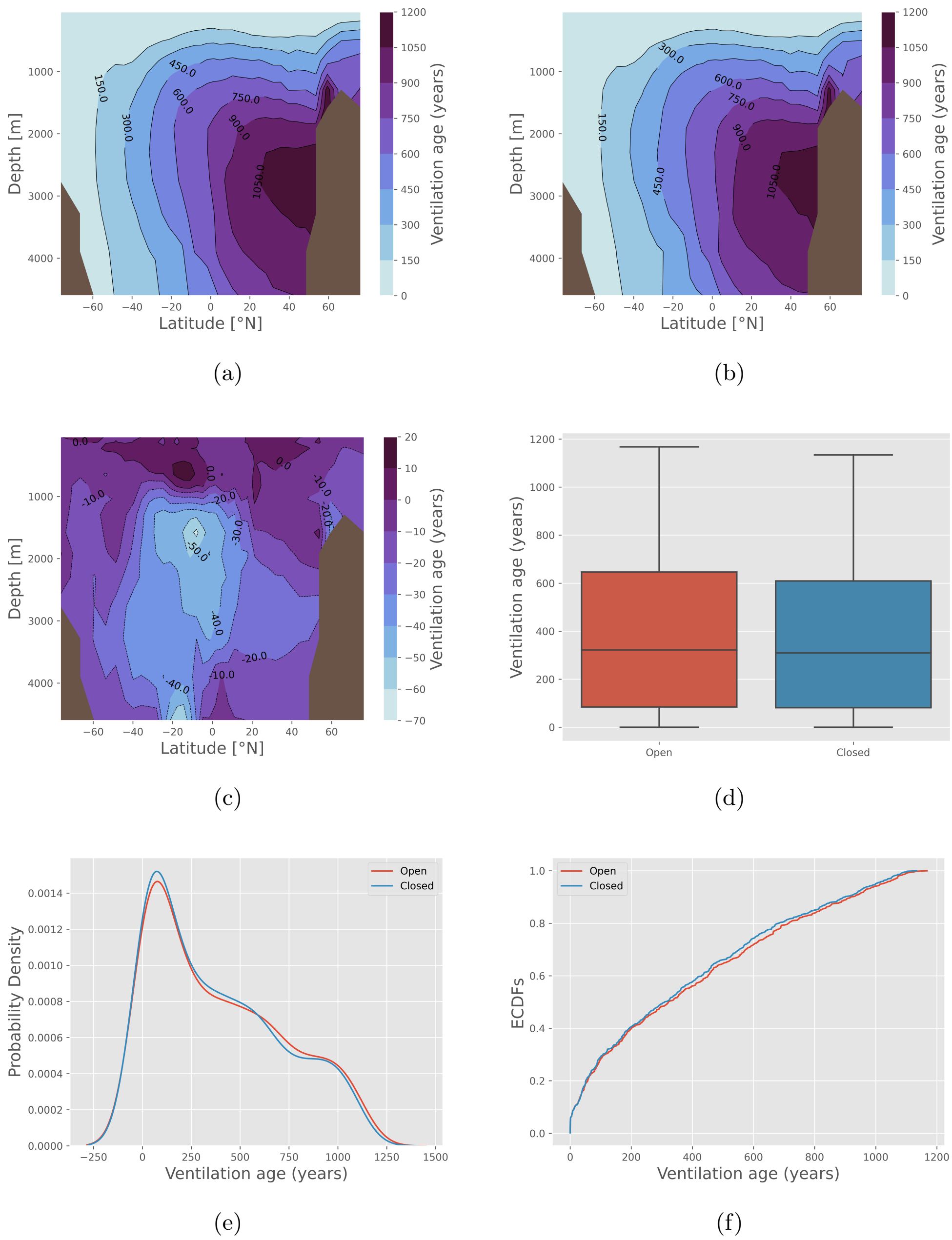

Fig. 4: Same as Figures 1, 2, and 3, but for zonally averaged ventilation age profiles.

Upon scrutinizing the four variables, our analysis discerned subtle differences that did not reach statistical significance. One plausible explanation for this outcome lies in the regional impact of the ITF. Notably, the ITF exerts a substantial influence on heat flux in specific regions, including the waters around Australia, the southern Indian Ocean, and the North and South Pacific [15, 17, 33]. Intriguingly, the heat transport generated by the ITF seems to dissipate into the atmosphere upon traversing the southwest Indian Ocean [15, 89].

This regional influence on surface oceanography becomes apparent in the strongest surface density anomalies observed after the closure of the IA, particularly in southern Mindanao (the ITF entry point from the North Pacific) and eastern Australia, where the ITF traditionally plays a pivotal role in shaping the East Australian Current (EAC) system [25, 33]. The vertical transect of the global density anomaly further highlights this, revealing a reduction in density at coordinates 21.17°N, possibly indicating the accumulation of surface flow from the North Pacific, impeded by the closure of the IA in the Philippine Sea. Similarly, the diminished vertical density anomaly at coordinates 11.21°S may be attributed to a reduced supply of warm and freshwater, a consequence of IA closure impacting the Indian Ocean.

Moving to the global overturning circulation, while no statistically significant changes were identified, anomalies in vertical transport, both clockwise and counterclockwise, were observed in the Southern Ocean, particularly around 40° - 60°S. These anomalies may be linked to a potential reduction in upwelling intensity from Indian Deep Water (IDW), Pacific Deep Water (PDW), NADW, and Antarctic Bottom Water (AABW) [90]. Furthermore, a reduction in ocean ventilation age in the same area suggests a potential decrease in the Agulhas Current intensity, subsequently impacting Agulhas Leakage and contributing to a slight reduction in NADW formation to the north [91]. It's essential to note that these speculations are limited by statistical insignificance and the constraints of cGENIE, an EMIC that does not account for mesoscale eddies influencing deep and intermediate water formation [92–94].

Drawing a comparison with the study conducted by Di Nezio et al. [95], where the Last Glacial Maximum (LGM) setting in the Community Earth System Model version 1.2 (CESM1) was employed, our findings provide additional nuances. Di Nezio et al. [95] identified a minimal reduction in the ITF, specifically 1.5 Sv, under conditions where the IA is nearly closed, allowing only ITF passage through the Makassar Strait and the Timor Gap.

It is noteworthy that transient interbasin exchange, a factor influencing energy transfer from the Indo-Pacific to the Atlantic [50, 96], was not incorporated into the numerical experiments we conducted . This aspect, albeit not explored in our study, has been acknowledged as a potentially pivotal contributor to the dynamics of the global THC. The intricate interplay of these transient interactions could unveil additional layers of complexity in understanding the broader implications of IA closure on global processes.

4 Conclusion

In conclusion, our 10,000-year simulation using the cGENIE Earth System Model reveals subtle regional variations in surface density, vertical profiles, global overturning circulation, and ventilation age following IA closure. However, statistical analysis indicates that these changes lack global significance. The study highlights the regional impact of ITF in areas such as southern Mindanao and eastern Australia.

Regarding NADW and AABW, our findings suggest potential alterations in upwelling and downwelling intensities and Agulhas Current dynamics in the Southern Ocean. However, these observations are speculative due to statistical insignificance and model constraints. The limitations of cGENIE are acknowledged, emphasizing the need for more sophisticated climate models. The study underscores the ongoing challenge of refining Earth System Models for a comprehensive understanding of complex interactions in global ocean dynamics and climate.

Declarations

Acknowledgments. We express profound gratitude to Andrew J. Ridgwell and Raden D. Susanto for enriching discussions and invaluable guidance in refining the numerical experiment setup.

Funding. This study received financial support from the Dean's Distinguished Fellowship at the University of California, Riverside, and the ITB Research, Community Service, and Innovation Program (PPMI-ITB).

Conflicts of interest/Competing interests. The authors declare no competing interests.

Data and Code availability. Explore the open-source Python code, cGENIE base and user configurations, and model outputs at https://github.com/sandyherho/globITFPhysGENIE. Obtain the cGENIE muffin version at https://github.com/derpycode/cgenie.muffin.

Author Contributions. All authors reviewed the manuscript and contributed equally to the manuscript.

References

[1] Hall R. In: Gillespie R, Clague D, editors. Indonesia, Geology. Berkeley: University of California Press; 2009. p. 454–460.

[2] Hall R, Cottam MA, Wilson MEJ. The SE Asian gateway: history and tectonics of the Australia–Asia collision. Geol Soc Spec Publ. 2011;355(1):1–6. https://doi.org/https://doi.org/10.1144/SP355.1.

[3] Hall R. The subduction initiation stage of the Wilson cycle. Geol Soc Spec Publ. 2019;470(1):415–437. https://doi.org/https://doi.org/10.1144/SP470.3.

[4] Ramage CS. ROLE OF A TROPICAL "MARITIME CONTINENT" IN THE ATMOSPHERIC CIRCULATION. Mon Weather Rev. 1968;96(6):365 – 370. https://doi.org/https://doi.org/10.1175/1520-0493(1968)096⟨0365:ROATMC⟩2.0.CO;2.

[5] De Deckker P. The Indo-Pacific Warm Pool: critical to world oceanography and world climate. Geosci Lett. 2016;3(1):1–12. https://doi.org/https://doi.org/10.1186/s40562-016-0054-3.

[6] Yamanaka MD. Physical climatology of Indonesian maritime continent: An outline to comprehend observational studies. Atmos Res. 2016;178-179:231–259. https://doi.org/https://doi.org/10.1016/j.atmosres.2016.03.017.

[7] Yang S, Zhang T, Li Z, Dong S. Climate variability over the Maritime Continent and its role in global climate variation: A review. J Meteorol Res. 2019;33(6):993–1015. https://doi.org/https://doi.org/10.1007/s13351-019-9025-x.

[8] Chang CP, Wang Z, McBride J, Liu CH. Annual cycle of Southeast Asia—Maritime Continent rainfall and the asymmetric monsoon transition. J Clim. 2005;18(2):287–301. https://doi.org/https://doi.org/10.1175/JCLI-3257.1.

[9] Bjerknes J. Atmospheric teleconnections from the equatorial Pacific. Mon Weather Rev. 1969;97(3):163–172. https://doi.org/https://doi.org/10.1175/1520-0493(1969)097⟨0163:ATFTEP⟩2.3.CO;2.

[10] Saji NH, Goswami BN, Vinayachandran PN, Yamagata T. A dipole mode in the tropical Indian Ocean. Nature. 1999;401(6751):360–363. https://doi.org/https://doi.org/10.1038/43854.

[11] Madden RA, Julian PR. Detection of a 40–50 day oscillation in the zonal wind in the tropical Pacific. J Atmos Sci. 1971;28(5):702–708. https://doi.org/https://doi.org/10.1175/1520-0469(1971)028⟨0702:DOADOI⟩2.0.CO;2.

[12] Wyrtki K. Physical oceanography of the Southeast Asia waters. NAGA report. 1961;2:1–195. https://doi.org/https://doi.org/10.1017/S0025315400054370.

[13] Gordon AL. Interocean exchange of thermocline water. J Geophys Res Oceans. 1986;91(C4):5037–5046. https://doi.org/https://doi.org/10.1029/JC092iC12p12941.

[14] Wyrtki K. Indonesian through flow and the associated pressure gradient. J Geophys Res Oceans. 1987;92(C12):12941–12946. https://doi.org/https://doi.org/10.1029/JC091iC04p05037.

[15] Godfrey JS. The effect of the Indonesian throughflow on ocean circulation and heat exchange with the atmosphere: A review. J Geophys Res Oceans. 1996;101(C5):12217–12237. https://doi.org/https://doi.org/10.1029/95JC03860.

[16] Schneider N. The Indonesian Throughflow and the global climate system. J Clim. 1998;11(4):676–689. https://doi.org/https://doi.org/10.1175/1520-0442(1998)011⟨0676:TITATG⟩2.0.CO;2.

[17] Godfrey JS, Golding TJ. The Sverdrup relation in the Indian Ocean, and the effect of Pacific-Indian Ocean throughflow on Indian Ocean circulation and on the East Australian Current. J Phys Oceanogr. 1981;11(6):771–779. https://doi.org/https://doi.org/10.1175/1520-0485(1981)011⟨0771:TSRITI⟩2.0.CO;2.

[18] Piola AR, Gordon AL. Pacific and Indian Ocean upper-layer salinity budget. J Phys Oceanogr. 1984;14(4):747–753. https://doi.org/https://doi.org/10.1175/1520-0485(1984)014⟨0747:PAIOUL⟩2.0.CO;2.

[19] Wunsch C, Hu D, Grant B. Mass, heat, salt and nutrient fluxes in the South Pacific Ocean. J Phys Oceanogr. 1983;13(5):725–753. https://doi.org/https://doi.org/10.1175/1520-0485(1983)013⟨0725:MHSANF⟩2.0.CO;2.

[20] Fine RA. Direct evidence using tritium data for throughflow from the Pacific into the Indian Ocean. Nature. 1985;315(6019):478–480. https://doi.org/https://doi.org/10.1038/315478a0.

[21] Fu LL. Mass, heat and freshwater fluxes in the South Indian Ocean. J Phys Oceanogr. 1986;16(10):1683–1693. https://doi.org/https://doi.org/10.1175/1520-0485(1986)016⟨1683:MHAFFI⟩2.0.CO;2.

[22] Murray SP, Arief D. Throughflow into the Indian Ocean through the Lombok Strait, January 1985–January 1986. Nature. 1988;333(6172):444–447. https://doi.org/https://doi.org/10.1038/333444a0.

[23] Godfrey JS. A Sverdrup model of the depth-integrated flow for the world ocean allowing for island circulations. Geophys Astrophys Fluid Dyn. 1989;45(1-2):89–112. https://doi.org/https://doi.org/10.1080/03091928908208894.

[24] Toole JM, Warren BA. A hydrographic section across the subtropical South Indian Ocean. Deep-Sea Res I: Oceanogr Res Pap. 1993;40(10):1973–2019. https://doi.org/https://doi.org/10.1016/0967-0637(93)90042-2.

[25] Hirst AC, Godfrey JS. The response to a sudden change in Indonesian throughflow in a global ocean GCM. J Phys Oceanogr. 1994;24(9):1895–1910. https://doi.org/https://doi.org/10.1175/1520-0485(1994)024⟨1895:TRTASC⟩2.0.CO;2.

[26] Molcard R, Fieux M, Swallow JC, Ilahude AG, Banjarnahor J. Low frequency variability of the currents in Indonesian channels (Savu-Roti and Roti-Ashmore Reef). Deep-Sea Res I: Oceanogr Res Pap. 1994;41(11-12):1643–1661. https://doi.org/https://doi.org/10.1016/0967-0637(94)90066-3.

[27] Miyama T, Awaji T, Akitomo K, Imasato N. Study of seasonal transport variations in the Indonesian seas. J Geophys Res Oceans. 1995;100(C10):20517–20541. https://doi.org/https://doi.org/10.1029/95JC01667.

[28] Shriver JF, Hurlburt HE. The contribution of the global thermohaline circulation to the Pacific to Indian Ocean Throughflow via Indonesia. J Geophys Res Oceans. 1997;102(C3):5491–5511. https://doi.org/https://doi.org/10.1029/96JC03602.

[29] Gordon AL, Susanto RD, Ffield A. Throughflow within Makassar Strait. Geophys Res Lett. 1999;26(21):3325–3328. https://doi.org/https://doi.org/10.1029/1999GL002340.

[30] Molcard R, Fieux M, Syamsudin F. The throughflow within Ombai Strait. Deep-Sea Res I: Oceanogr Res Pap. 2001;48(5):1237–1253. https://doi.org/https://doi.org/10.1016/S0967-0637(00)00084-4.

[31] Song Q, Vecchi GA, Rosati AJ. The role of the Indonesian Throughflow in the Indo–Pacific climate variability in the GFDL Coupled Climate Model. J Clim. 2007;20(11):2434–2451. https://doi.org/https://doi.org/10.1175/JCLI4133.1.

[32] van Sebille E, Sprintall J, Schwarzkopf FU, Sen Gupta A, Santoso A, England MH, et al. Pacific-to-Indian Ocean connectivity: Tasman leakage, Indonesian Throughflow, and the role of ENSO. J Geophys Res Oceans. 2014;119(2):1365–1382. https://doi.org/https://doi.org/10.1002/2013JC009525.

[33] Feng M, Zhang N, Liu Q, Wijffels S. The Indonesian throughflow, its variability and centennial change. Geosci Lett. 2018;5(1):1–10. https://doi.org/https://doi.org/10.1186/s40562-018-0102-2.

[34] Gordon AL. Oceanography of the Indonesian Seas and Their Throughflow. Oceanography. 2005;18(4):14. https://doi.org/https://doi.org/10.5670/oceanog.2005.01.

[35] Schiller A, Wijffels SE, Sprintall J. Variability of the Indonesian Throughflow: a review and model-to-data comparison. Elsevier Oceanogr Ser. 2007;73:175–494. https://doi.org/https://doi.org/10.1016/S0422-9894(06)73008-2.

[36] Sprintall J, Gordon AL, Koch-Larrouy A, Lee T, Potemra JT, Pujiana K, et al. The Indonesian seas and their role in the coupled ocean–climate system. Nat Geosci. 2014;7(7):487–492. https://doi.org/https://doi.org/10.1038/ngeo2188.

[37] Sen Gupta A, McGregor S, van Sebille E, Ganachaud A, Brown JN, Santoso A. Future changes to the Indonesian Throughflow and Pacific circulation: The differing role of wind and deep circulation changes. Geophys Res Lett. 2016;43(4):1669–1678. https://doi.org/https://doi.org/10.1002/2016GL067757.

[38] Feng M, Zhang X, Sloyan B, Chamberlain M. Contribution of the deep ocean to the centennial changes of the Indonesian Throughflow. Geophys Res Lett. 2017;44(6):2859–2867. https://doi.org/https://doi.org/10.1002/2017GL072577.

[39] Hughes TMC, Weaver AJ, Godfrey JS. Thermohaline forcing of the Indian Ocean by the Pacific Ocean. Deep-Sea Res Part A Oceanogr Res Pap. 1992;39(6):965–995. https://doi.org/https://doi.org/10.1016/0198-0149(92)90035-R.

[40] Broecker WS. The Great Ocean Conveyor. Oceanography. 1991;4(2):79–89. https://doi.org/https://doi.org/10.5670/oceanog.1991.07.

[41] Barker S, Knorr G, Conn S, Lordsmith S, Newman D, Thornalley D. Early interglacial legacy of deglacial climate instability. Paleoceanogr Paleoclimatol. 2019;34(8):1455–1475. https://doi.org/https://doi.org/10.1029/2019PA003661.

[42] Corrick EC, Drysdale RN, Hellstrom JC, Capron E, Rasmussen SO, Zhang X, et al. Synchronous timing of abrupt climate changes during the last glacial period. Science. 2020;369(6506):963–969. https://doi.org/https://doi.org/10.1126/science.aay8178.

[43] Lohmann G, Butzin M, Eissner N, Shi X, Stepanek C. Abrupt climate and weather changes across time scales. Paleoceanogr Paleoclimatol. 2020;35(9):e2019PA003782. https://doi.org/https://doi.org/10.1029/2019PA003782.

[44] Yin QZ, Wu ZP, Berger A, Goosse H, Hodell D. Insolation triggered abrupt weakening of Atlantic circulation at the end of interglacials. Science. 2021;373(6558):1035–1040. https://doi.org/https://doi.org/10.1126/science.abg1737.

[45] Boers N, Ghil M, Stocker TF. Theoretical and paleoclimatic evidence for abrupt transitions in the Earth system. Environ Res Lett. 2022;17(9):093006. https://doi.org/10.1088/1748-9326/ac8944.

[46] Haskins RK, Oliver KIC, Jackson LC, Wood RA, Drijfhout SS. Temperature domination of AMOC weakening due to freshwater hosing in two GCMs. Clim Dyn. 2020;54:273–286. https://doi.org/https://doi.org/10.1007/s00382-019-04998-5.

[47] Bonnet R, Swingedouw D, Gastineau G, Boucher O, Deshayes J, Hourdin F, et al. Increased risk of near term global warming due to a recent AMOC weakening. Nat Commun. 2021;12(1):6108. https://doi.org/https://doi.org/10.1029/2020GL090615.

[48] Baker JA, Bell MJ, Jackson LC, Renshaw R, Vallis GK, Watson AJ, et al. Overturning pathways control AMOC weakening in CMIP6 models. Geophys Res Lett. 2023;50(14):e2023GL103381. https://doi.org/https://doi.org/10.1029/2023GL103381.

[49] Madan G, Gjermundsen A, Iversen SC, LaCasce JH. The weakening AMOC under extreme climate change. Clim Dyn. 2023;p. 1–19. https://doi.org/https://doi.org/10.1007/s00382-023-06957-7.

[50] Sun S, Thompson AF. Centennial changes in the Indonesian throughflow connected to the Atlantic meridional overturning circulation: The Ocean's transient conveyor belt. Geophys Res Lett. 2020;47(21):e2020GL090615. https://doi.org/https://doi.org/10.1029/2020GL090615.

[51] Sprintall J, Gordon AL, Wijffels SE, Feng M, Hu S, Koch-Larrouy A, et al. Detecting Change in the Indonesian Seas. Front Mar Sci. 2019;6. https://doi.org/10.3389/fmars.2019.00257.

[52] Lee T, Fukumori I, Menemenlis D, Xing Z, Fu LL. Effects of the Indonesian throughflow on the Pacific and Indian Oceans. J Phys Oceanogr. 2002;32(5):1404–1429. https://doi.org/https://doi.org/10.1175/1520-0485(2002)032⟨1404:EOTITO⟩2.0.CO;2.

[53] Pandey VK, Bhatt V, Pandey AC, Das IML. Impact of Indonesian throughflow blockage on the Southern Indian Ocean. Curr Sci. 2007;p. 399–406.

[54] Wang J, Yuan D, Zhao X. Impacts of Indonesian Throughflow on seasonal circulation in the equatorial Indian Ocean. Chin J Oceanol Limnol. 2017;35(6):1261–1274. https://doi.org/https://doi.org/10.1007/s00343-017-6196-0.

[55] Marsh R, Müller SA, Yool A, Edwards NR. Incorporation of the C-GOLDSTEIN efficient climate model into the GENIE framework: "eb_go_gs" configurations of GENIE. Geosci Model Dev. 2011;4(4):957–992. https://doi.org/10.5194/gmd-4-957-2011.

[56] Claussen M, Mysak L, Weaver A, Crucifix M, Fichefet T, Loutre MF, et al. Earth system models of intermediate complexity: closing the gap in the spectrum of climate system models. Clim Dyn. 2002;18:579–586. https://doi.org/https://doi.org/10.1007/s00382-001-0200-1.

[57] Weber SL. The utility of Earth system Models of Intermediate Complexity (EMICs). Wiley Interdiscip Rev Clim Change. 2010;1(2):243–252. https://doi.org/https://doi.org/10.1002/wcc.24.

[58] Lenton TM, Williamson MS, Edwards NR, Marsh R, Price AR, Ridgwell AJ, et al. Millennial timescale carbon cycle and climate change in an efficient Earth system model. Clim Dyn. 2006;26:687–711. https://doi.org/https://doi.org/10.1007/s00382-006-0109-9.

[59] Edwards NR, Marsh R. Uncertainties due to transport-parameter sensitivity in an efficient 3-D ocean-climate model. Clim Dyn. 2005;24:415–433. https://doi.org/https://doi.org/10.1007/s00382-004-0508-8.

[60] Ridgwell A, Hargreaves JC, Edwards NR, Annan JD, Lenton TM, Marsh R, et al. Marine geochemical data assimilation in an efficient Earth System Model of global biogeochemical cycling. Biogeosciences. 2007;4(1):87–104. https://doi.org/https:

//doi.org/10.5194/bg-4-87-2007.

[61] Williamson MS, Lenton TM, Shepherd JG, Edwards NR. An efficient numerical terrestrial scheme (ENTS) for fast Earth system modelling. Tyndall Centre Working Paper 83; 2006.

[62] Colbourn G, Ridgwell A, Lenton TM. The Rock Geochemical Model (RokGeM) v0.9. Geosci Model Dev. 2013;6(5):1543–1573. https://doi.org/10.5194/gmd-6-1543-2013.

[63] Ridgwell A, Hargreaves JC. Regulation of atmospheric CO_2 by deep-sea sediments in an Earth system model. Glob Biogeochem Cycles. 2007;21(2). https://doi.org/https://doi.org/10.1029/2006GB002764.

[64] Ward BA, Wilson JD, Death RM, Monteiro FM, Yool A, Ridgwell A. EcoGEnIE 1.0: plankton ecology in the cGEnIE Earth system model. Geosci Model Dev. 2018;11(10):4241–4267. https://doi.org/10.5194/gmd-11-4241-2018.

[65] Holden PB, Edwards NR, Fraedrich K, Kirk E, Lunkeit F, Zhu X. PLASIM–GENIE v1.0: a new intermediate complexity AOGCM. Geosci Model Dev. 2016;9(9):3347–3361. https://doi.org/10.5194/gmd-9-3347-2016.

[66] Evensen G. The ensemble Kalman filter: Theoretical formulation and practical implementation. Ocean Dyn. 2003;53:343–367. https://doi.org/https://doi.org/10.1007/s10236-003-0036-9.

[67] Edwards NR, Willmott AJ, Killworth PD. On the role of topography and wind stress on the stability of the thermohaline circulation. J Phys Oceanogr. 1998;28(5):756–778. https://doi.org/https://doi.org/10.1175/1520-0485(1998)028⟨0756:OTROTA⟩2.0.CO;2.

[68] Edwards N, Shepherd J. Bifurcations of the thermohaline circulation in a simplified three-dimensional model of the world ocean and the effects of inter-basin connectivity. Clim Dyn. 2002;19:31–42. https://doi.org/https://doi.org/10.1007/s00382-001-0207-7.

[69] Lenton TM, Myerscough RJ, Marsh R, Livina VN, Price AR, Cox SJ, et al. Using GENIE to study a tipping point in the climate system. Philos Trans Royal Soc A. 2009;367(1890):871–884. https://doi.org/https://doi.org/10.1098/rsta.2008.0171.

[70] Weaver AJ, Eby M, Wiebe EC, Bitz CM, Duffy PB, Ewen TL, et al. The UVic Earth System Climate Model: Model Description, Climatology, and Applications to Past, Present and Future Climates. Atmos - Ocean. 2001;39(4):361–428. https://doi.org/https://doi.org/10.1080/07055900.2001.9649686.

[71] Manabe S, Bryan K. Climate Calculations with a Combined Ocean-Atmosphere Model. J Atmos Sci. 1969;26(4):786–789. https://doi.org/https://doi.org/10.1175/1520-0469(1969)026⟨0786:CCWACO⟩2.0.CO;2.

[72] Cao L, Eby M, Ridgwell A, Caldeira K, Archer D, Ishida A, et al. The role of ocean transport in the uptake of anthropogenic CO_2. Biogeosciences. 2009;6(3):375–390. https://doi.org/10.5194/bg-6-375-2009.

[73] Collins M, Tett S, Cooper C. The internal climate variability of HadCM3, a version of the Hadley Centre coupled model without flux adjustments. Clim Dyn. 2001;17:61–81. https://doi.org/https://doi.org/10.1007/s003820000094.

[74] Ridgwell A.: muffingen, 0.9.30. Zenodo; 2022. Available from: https://doi.org/10.5281/zenodo.6676451.

[75] England MH. The Age of Water and Ventilation Timescales in a Global Ocean Model. J Phys Oceanogr. 1995;25(11):2756–2777. https://doi.org/https://doi.org/10.1175/1520-0485(1995)025⟨2756:TAOWAV⟩2.0.CO;2.

[76] Sura P, Sardeshmukh PD. A global view of non-Gaussian SST variability. J Phys Oceanogr. 2008;38(3):639–647. https://doi.org/https://doi.org/10.1175/2007JPO3761.1.

[77] Jiang X, Zhang T, Gao D, Wang D, Yang Y. Estimating the evolution of sea state non-Gaussianity based on a phase-resolving model. J Oceanol Limnol. 2022;40(5):1909–1923. https://doi.org/https://doi.org/10.1007/s00343-021-1236-1.

[78] Pagniello CMLS, Maoiléidigh N, Maxwell H, Castleton MR, Aalto EA, Dale JJ, et al. Tagging of Atlantic bluefin tuna off Ireland reveals use of distinct oceanographic hotspots. Prog Oceanogr. 2023;219:103135. https://doi.org/https://doi.org/10.1016/j.pocean.2023.103135.

[79] Herho SHS, Herho KEP, Susanto RD. Did hydroclimate conditions contribute to the political dynamics of Majapahit? A preliminary analysis. Geogr Pannonica. 2023;27(3):199–210. https://doi.org/https://doi.org/10.5937/gp27-44682.

[80] Varona HL, Noriega C, Araujo J, Lira S, Araujo M. mStatGraph: Exploration and statistical treatment software to process, compute and validate oceanographic data. Softw Impacts. 2023;17:100571. https://doi.org/https://doi.org/10.1016/j.simpa.2023.100571.

[81] Shanks AL, Rasmuson LK, Valley JR, Jarvis MA, Salant C, Sutherland DA, et al. Marine heat waves, climate change, and failed spawning by coastal invertebrates. Limnol Oceanogr. 2020;65(3):627–636. https://doi.org/https://doi.org/10.1002/lno.11331.

[82] Lanzante JR. Testing for differences between two distributions in the presence of serial correlation using the Kolmogorov–Smirnov and Kuiper's tests. Int J Climatol. 2021;41(14):6314–6323. https://doi.org/https://doi.org/10.1002/joc.7196.

[83] Galli M, Baini M, Panti C, Giani D, Caliani I, Campani T, et al. Oceanographic and anthropogenic variables driving marine litter distribution in Mediterranean protected areas: Extensive field data supported by forecasting modelling. Sci Total Environ. 2023;903:166266. https://doi.org/https://doi.org/10.1016/j.scitotenv.2023.16.

[84] Hoyer S, Hamman J. xarray: ND labeled arrays and datasets in Python. J Open Res Softw. 2017;5(1). https://doi.org/https://doi.org/10.5334/jors.148.

[85] van der Walt S, Colbert S, Varoquaux G. The NumPy Array: A Structure for Efficient Numerical Computation. Comput Sci Eng. 2011;13(2):22–30. https://doi.org/https://doi.org/10.1109/MCSE.2011.37.

[86] Virtanen P, Gommers R, Oliphant TE, Haberland M, Reddy T, Cournapeau D, et al. SciPy 1.0: fundamental algorithms for scientific computing in Python. Nat Methods. 2020;17(3):261–272. https://doi.org/https://doi.org/10.1038/s41592-019-0686-2.

[87] Hunter JD. Matplotlib: A 2D graphics environment. Comput Sci Eng. 2007;9(3):90–95. https://doi.org/https://doi.org/10.1109/MCSE.2007.55.

[88] Waskom ML. seaborn: statistical data visualization. Journal of Open Source Software. 2021;6(60):3021. https://doi.org/https://doi.org/10.21105/joss.03021.

[89] Vranes K, Gordon AL, Ffield A. The heat transport of the Indonesian Throughflow and implications for the Indian Ocean heat budget. Deep-Sea Res Part II Top Stud Oceanogr. 2002;49(7-8):1391–1410. https://doi.org/https://doi.org/10.1016/S0967-0645(01)00150-3.

[90] Talley LD. Shallow, Intermediate, and Deep Overturning Components of the Global Heat Budget. J Phys Oceanogr. 2003;33(3):530–560. https://doi.org/https://doi.org/10.1175/1520-0485(2003)033⟨0530:SIADOC⟩2.0.CO;2.

[91] Durgadoo JV, Rühs S, Biastoch A, Böning CW. Indian Ocean sources of Agulhas leakage. J Geophys Res Oceans. 2017;122(4):3481–3499. https://doi.org/https://doi.org/10.1002/2016JC012676.

[92] Böning CW, Bryan FO, Holland WR, Döscher R. Deep-water formation and meridional overturning in a high-resolution model of the North Atlantic. J Phys Oceanogr. 1996;26(7):1142–1164.

[93] Lachkar Z, Orr JC, Dutay JC, Delecluse P. On the role of mesoscale eddies in the ventilation of Antarctic intermediate water. Deep-Sea Res I: Oceanogr Res Pap. 2009;56(6):909–925. https://doi.org/https://doi.org/10.1016/j.dsr.2009.01.013.

[94] Manta G, Speich S, Karstensen J, Hummels R, Kersalé M, Laxenaire R, et al. The South Atlantic meridional overturning circulation and mesoscale eddies in the first GO-SHIP section at 34.5° S. J Geophys Res Oceans. 2021;126(2):e2020JC016962. https://doi.org/https://doi.org/10.1029/2020JC016962.

[95] Di Nezio PN, Timmermann A, Tierney JE, Jin FF, Otto-Bliesner B, Rosenbloom N, et al. The climate response of the Indo-Pacific warm pool to glacial sea level. Paleoceanography. 2016;31(6):866–894. https://doi.org/https://doi.org/10.1002/2015PA002890.

[96] Sun S, Thompson AF, Eisenman I. Transient overturning compensation between Atlantic and Indo-Pacific basins. J Phys Oceanogr. 2020;50(8):2151–2172. https://doi.org/https://doi.org/10.1175/JPO-D-20-0060.1.